Magnetic properties of transition-metal multilayers studied with X-ray magnetic circular dichroism spectroscopy

by J. Stöhr
R. Nakajima

The detailed understanding of the magnetic properties of transition-metal multilayers requires the use of state-of-the-art experimental techniques. Over the last few years, the X-ray magnetic circular dichroism (XMCD) technique has evolved into an important magnetometry tool. This paper is an overview of the principles and unique strengths of the technique. Aspects covered include the quantitative determination of element-specific spin and orbital magnetic moments and their anisotropies through sum-rule analyses of experimental spectra. A discussion is presented on how the spin and orbital magnetic moments in transition-metal thin films and sandwiches are modified relative to the bulk. We show that a thin film of a nonmagnetic metal such as Cu may become magnetically active when adjacent to a magnetic layer, and a thin film of a ferromagnetic metal such as Fe may become magnetically inactive. The orbital moment is found to become anisotropic in thin films; it can be regarded as the microscopic origin of the magnetocrystalline anisotropy.

1. Introduction

Research on magnetism has undergone a renaissance over the last decade, following the discovery of a variety of new scientific phenomena associated with artificially fabricated thin transition-metal films. Among the advances that have occurred are the theoretical prediction of enhanced magnetic moments in ultrathin films and at surfaces [1], the discovery of perpendicular magnetic anisotropy (PMA) in layered structures [2, 3], and the discoveries of the giant magnetoresistance effect [4, 5] and oscillatory exchange coupling [6] in multilayers achieved by alternating magnetic and "nonmagnetic" metals. Some of these discoveries are expected to have a major impact on

©**Copyright** 1998 by International Business Machines Corporation. Copying in printed form for private use is permitted without payment of royalty provided that (1) each reproduction is done without alteration and (2) the *Journal* reference and IBM copyright notice are included on the first page. The title and abstract, but no other portions, of this paper may be copied or distributed royalty free without further permission by computer-based and other information-service systems. Permission to *republish* any other portion of this paper must be obtained from the Editor.

0018-8646/98/$5.00 © 1998 IBM

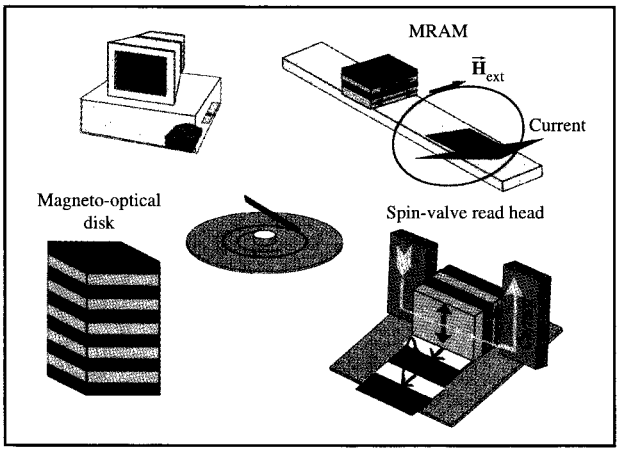

Figure 1

Several potential applications of transition-metal multilayers in information technology, as discussed in the text.

information technology. Several potential applications are shown in **Figure 1**. Magneto-optical recording involves writing and reading of magnetic domains or "bits" by use of a polarized focused laser beam and a magnetic thin film, or "medium," on a disk. Focused laser light is used in both the writing and reading processes, and the bit size is determined by the size of the laser spot. The magnetic medium must have an easy magnetization direction perpendicular to the film surface, because the magnetization directions of the bits are read by means of the magneto-optical Kerr effect, using a normal incidence geometry of the laser light. Since the achievable spot size depends on the laser wavelength (i.e., is determined by the diffraction limit), it is desirable to use "blue" rather than conventional "red" lasers in order to increase the bit density on the disk. Co/Pt or Co/Pd multilayers with PMA show promise as "blue" magneto-optical media because of their enhanced Kerr response at blue laser wavelengths compared to conventional TbCoFe films [7]. Such multilayers, and Co/Au, discussed later in this paper, are found to exhibit the desired perpendicular magnetic anisotropy for layer thicknesses around 10 Å. Spin-valve sensors based on the giant magnetoresistance (GMR) effect are expected to replace conventional $Ni_{80}Fe_{20}$ (permalloy) films in magnetic read heads because of their increased sensitivity [8, 9]. In their simplest form, spin-valve read heads consist of two ferromagnetic layers, separated by a nonmagnetic layer, e.g., a Cu layer. The magnetization direction in one of the ferromagnetic layers is pinned by exchange coupling to an antiferromagnet, for example FeMn or NiO, while the magnetization direction in the other ferromagnetic layer may be rotated by the weak magnetic field originating from the magnetic bits of the magnetic disk which rotates underneath the head. As shown in Figure 1, the bits in magnetic recording media are typically magnetized "in-plane," while the magnetic flux experienced by the head is in the "out-of-plane" direction. A current flowing through the spin-valve structure experiences a resistance which depends on the relative orientation of the magnetization directions in the two ferromagnetic layers. This change in resistance, of the order of a few percent, is the origin of the sensor signal of a spin-valve magnetic recording head. Spin-valve-like structures also promise nonvolatile alternatives (the information is stored in magnetic bits which survive power failures) to semiconductor-based dynamic random access memories (DRAMs) [10–12]. The magnetic random access memory (MRAM) cell shown in the figure has a spin-valve-like structure. The memory bits consist of parallel or antiparallel orientations of the magnetization directions in the two ferromagnetic layers. A bit is written by the magnetic field of a current flowing through a lithographically created adjacent "wire." The memory bit is read by a current flowing through the cell, as in the spin-valve read head. As indicated in the figure, many of the materials of technological interest are in the form of artificially layered structures, each layer consisting of a different metal, a few atomic layers thick. Because of the complexity of the materials and the small concentration of some components, state-of-the-art characterization techniques are needed to address scientific and technological issues.

X-ray magnetic circular dichroism (XMCD) spectroscopy, first suggested by Erskine and Stern [13] and pioneered by Schütz and coworkers in both the near-edge [14] and extended fine-structure regimes [15], is one of those techniques. It has several capabilities that are not afforded by traditional magnetics analysis techniques [16]. Its foremost strengths are the element-specific, quantitative determination of spin and orbital magnetic moments and their anisotropies. Other strengths are its chemical sensitivity [17], its element-specific imaging capability [18], and its submonolayer sensitivity [19–21]. In this paper we elucidate the basic concepts of near-edge XMCD. We keep the mathematical treatment to a minimum and use simple models to depict underlying physical processes. We emphasize the quantitative nature of the XMCD technique, which is based on sum-rule analyses of measured intensities. For this reason a thorough discussion of the sum rules is given. Finally, we present two applications of XMCD in the area of thin-film magnetism, illustrating the uniqueness of the technique for the quantitative determination of element-specific magnetic moments and their anisotropies. In particular, we show why the sensor signal in Ni/Fe/Cu/Fe/Ni spin valves can be greatly diminished by a change in the

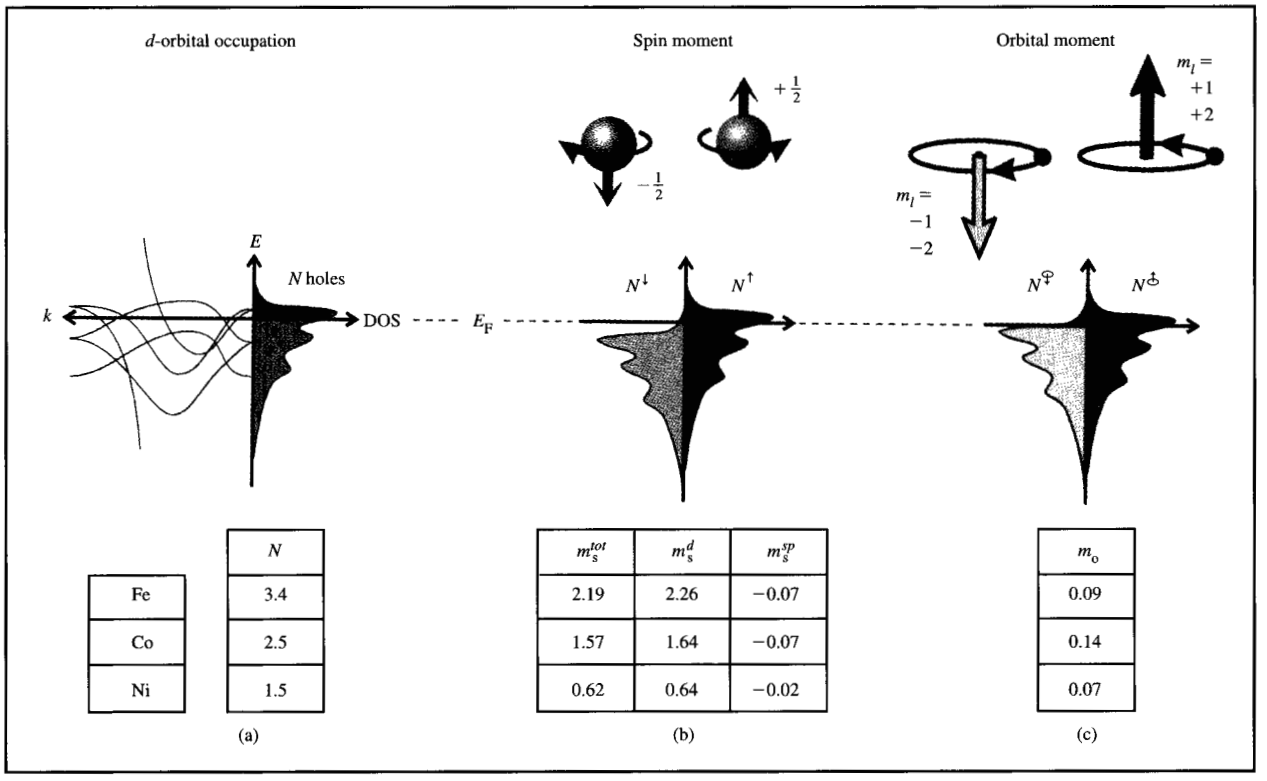

	N
Fe	3.4
Co	2.5
Ni	1.5

m_s^{tot}	m_s^d	m_s^{sp}
2.19	2.26	−0.07
1.57	1.64	−0.07
0.62	0.64	−0.02

m_o
0.09
0.14
0.07

Figure 2

Origin and definition of *d*-shell occupation (a), spin moment (b), and orbital moment (c) in a ferromagnetic transition metal. The tabulated values for Fe, Co, and Ni are from calculations of Eriksson et al. [22, 23].

magnetic properties of the Fe interfacial layers. We describe studies of Au/Co/Au sandwiches involving the use of angle-dependent XMCD spectroscopy in large external magnetic fields and the sum-rule separation of the spin and orbital parts of the magnetic moment. The studies have led to a relatively simple view of the origin of the magnetocrystalline anisotropy.

2. Magnetism in 3*d* transition metals

The magnetic properties of the 3*d* transition metals are determined primarily by their *d* valence electrons [22, 23], as illustrated in **Figure 2** for Fe, Co, and Ni. The figure illustrates that the summation of the *k*-dependent states over the Brillouin zone results in an energy-dependent density of states (DOS). All of the states below the Fermi level, denoted E_F, are filled. In going from Fe to Ni, the Fermi level moves toward the top of the *d* band, resulting in a decrease in the number of *d* holes, *N*, i.e., in the number of *d* states above the Fermi level. The origin of the magnetic spin moment is most easily understood in the rigid-band or Stoner model of ferromagnetism. The exchange interaction leads to an exchange splitting between the centers of gravity of the spin-up ($m_s = +\frac{1}{2}$) and spin-down ($m_s = -\frac{1}{2}$) subbands, and the magnitude of the spin magnetic moment [in units of Bohr magnetons (μ_B)] is simply the difference between the number of spin-up electrons and spin-down electrons. Since the imbalance in the filled states (electrons) is the same as that in the empty states (holes), one may also use a hole picture to define the magnetic moment. Note, however, that the direction of the magnetic moment is parallel to the majority hole spins while it is antiparallel to the majority electron spins [24]. For the case shown in Figure 2(b), the magnetic moment is given by $m_s = (N^\uparrow - N^\downarrow)\mu_B$ and it points in the up direction. Figure 2(b) shows that the spin moment originates nearly entirely from the *d* shell, the combined 4*s*/4*p* contribution being less than 5%. Figure 2(c) illustrates that the orbital moment arises from the difference in the number of holes with quantum numbers $m_l = +1, +2$ and $m_l = -1, -2$. Its value is proportional to the spin-orbit interaction, which breaks the time-reversal symmetry of electrons orbiting in opposite directions around the nucleus, as shown. Since the spin-orbit interaction is significantly smaller (a few meV) than

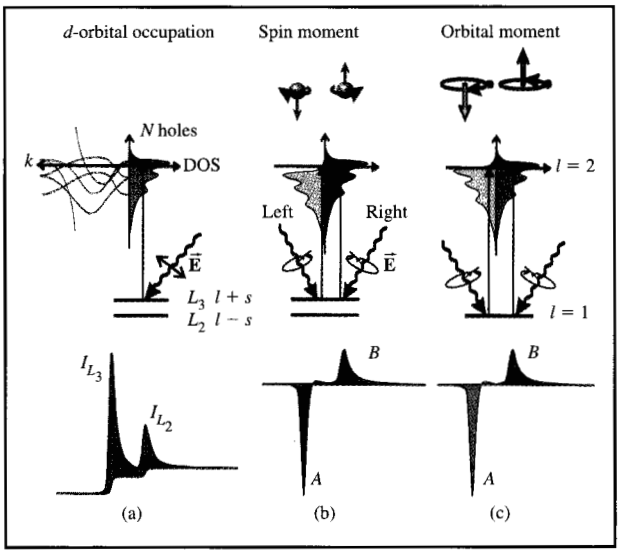

Figure 3

Electronic transitions in conventional L-edge X-ray absorption (a) (see Footnote 1), and in X-ray magnetic circular dichroism (b, c), illustrated in a one-electron model. The transitions occur from the spin-orbit split $2p$ core shell to empty conduction band states above the Fermi level E_F. In conventional X-ray absorption, the transition intensity measured as the white-line intensity $I_{L_3} + I_{L_2}$ is proportional to the number of d holes, N. By use of circularly polarized X-rays, the spin moment (b) and orbital moment (c) can be determined from the dichroic difference intensities A and B, as explained in the text.

the exchange interaction (~1 eV), the orbital moment is much smaller than the spin moment. The total magnetic moment is simply the sum of the spin and orbital parts. Despite its small absolute value, the orbital moment plays a crucial role in magnetism, as is discussed below. The tabulated moment values given in the figure are from calculations by Eriksson et al. [22, 23].

3. Basic concepts of XMCD spectroscopy

The properties of $3d$ electrons are best probed in an X-ray absorption experiment by excitation of $2p$ core electrons to unfilled $3d$ states, as illustrated by a simple one-electron case,[1] as depicted in Figure 3(a) [24]. In principle, L-edge X-ray absorption spectra contain contributions from both $p \rightarrow d$ and $p \rightarrow s$ transitions, but in practice the $p \rightarrow d$ channel dominates by a factor greater than 20 [25]. The L-edge absorption spectra are characterized by strong absorption resonances, so-called white lines, near the L_3 and L_2 thresholds. The sum of the white-line intensities, denoted I_{L_3} and I_{L_2}, respectively, is directly proportional to the number of d holes, as shown in **Figure 4**.[2] This correlation follows from one of several intensity sum rules [28–30] to be discussed below. Figure 4 also demonstrates the elemental specificity afforded by X-rays, because the L-edge position varies strongly with atomic number.

The use of circularly polarized X-rays opens the door for X-ray-based spectroscopy studies of magnetic materials and structures. The basis of XMCD spectroscopy is easily understood if we assume that the d shell has only a spin moment. In order to measure the difference in the number of d holes with up and down spin, we need to make the X-ray absorption process spin-dependent. Since spin flips are forbidden in electric dipole transitions governing X-ray absorption, spin-up (spin-down) photoelectrons from the p core shell can only be excited into spin-up (spin-down) d hole states. Hence, if one could preferentially generate spin-up photoelectrons in one measurement and spin-down ones in another, the difference in the transition intensity would simply reflect the difference in up and down holes in the d shell, i.e., the spin moment. This can be accomplished by the use of right- or left-circularly-polarized photons; the underlying physical mechanisms are most easily understood in the following two-step picture [24, 31].

- *Two-step model*

In the *first step*, right- or left-circularly-polarized photons transfer their angular momentum, $\hbar$ and $-\hbar$, respectively, to the excited photoelectron. The photoelectron carries the transferred angular momentum as a spin or an angular momentum [32], or both. If the photoelectron originates from a spin-orbit split level, e.g., the $p_{3/2}$ level (L_3 edge), its angular momentum can be transferred in part to the spin through the spin-orbit coupling. Right-circularly-polarized photons transfer to the electron a momentum opposite to that from left-circularly-polarized photons; hence, photoelectrons with opposite spins are created in the two cases. Since the $p_{3/2}$ (L_3) and $p_{1/2}$ (L_2) levels have opposite spin-orbit coupling ($l + s$ and $l - s$, respectively) the spin polarization will be opposite at the two edges. In the first (absorption) step, spin-up and spin-down are defined relative to the photon helicity or photon spin, which is parallel (right) or antiparallel (left) to the X-ray propagation direction [33].

The magnetic properties enter in the *second step*. Here the spin-split valence shell acts as a detector for the spin of the excited photoelectron. The quantization axis of the detector is given by the magnetization direction which, for

[1] The one-electron diagram shown in **Figure 3** is misleading, especially to the photoemission community, because it depicts the spin-orbit splitting of the p core shell as an "initial-state" effect. In the proper description based on a *configuration model*, an atom is excited from a ground or initial-state configuration to an excited or final-state configuration. While in general the one-electron and configuration models are not equivalent, equivalence does exist for the case of a d^9 ground state, as discussed elsewhere [24]. This, in fact, justifies use of the one-electron model.

[2] In the figure, TEY denotes total electron yield. One megabarn (Mb) is equal to 10^{-18} cm^2.

maximum dichroism effect, must be aligned with the photon spin direction. As illustrated in Figure 3(b), we denote the differences of the white-line intensities recorded with right- and left-circular polarization (i.e., the XMCD intensities) as A (L_3 edge) and B (L_2 edge), respectively. Note that A and B have opposite signs, reflecting the opposite spin-orbit coupling of the $p_{3/2}$ and $p_{1/2}$ levels. A powerful sum rule [29] links the spin moment quantitatively to the measured intensity $A - 2B$, as discussed below.

Similarly, if the d valence shell possesses an orbital moment, as shown in Figure 3(c), it acts as an orbital momentum detector for the excited photoelectron. Absorption of right- or left-circularly-polarized photons by a core shell always results in the production of photoelectrons with finite orbital momenta, even in the absence of spin-orbit coupling in the core. By summing over the L_3 ($l + s$) and L_2 ($l - s$) intensities, it is apparent that the spin s is eliminated and one measures the orbital moment of the valence shell, as schematically shown in Figure 3(c). This is expressed by the orbital moment sum rule [28], which links the orbital moment in the d shell to the dichroism intensity $A + B$. Since A and B have opposite signs, the existence of an orbital moment is readily revealed by different magnitudes of A and B.

In the above discussion we have assumed that the magnetization direction is fixed so that the XMCD intensity is the difference intensity, obtained for two X-ray helicities. It is easy to show that it is equivalent to keeping the X-ray helicity fixed and switching the magnetization direction [24].

4. Probing anisotropic charge and magnetic properties

So far we have implicitly assumed that the white-line and dichroism intensities do not depend on the sample orientation relative to the X-ray wave vector or polarization. This is a rather good approximation for the bulk 3d transition metals, which have high-symmetry lattices (fcc, bcc, or hcp); hence, the bonding and charge distribution is rather isotropic. If one describes the electronic band states in terms of basis functions consisting of the five d orbitals [34, 35], d_{xy}, d_{xz}, d_{yz}, $d_{x^2-y^2}$, and $d_{3z^2-r^2}$, one may define d-orbital projected quantities after summing over the Brillouin zone (BZ). For the bulk 3d metals, one then finds that the number of holes in states with different d-orbital symmetries is nearly identical. Another way of stating this result is to say that the charge density in the Wigner–Seitz cell is nearly isotropic. Similarly, the spin density and the orbital moment are rather isotropic.

For ultrathin films or surfaces, on the other hand, the intrinsic structural anisotropy results in different contributions from in-plane and out-of-plane orbitals, as shown in **Figure 5**. If the in-plane bonding is stronger than the out-of-plane bonding, for example, one would expect a larger in-plane than out-of-plane bandwidth. As shown in Figure 5, this results in different hole populations $N^{\parallel}$ and $N^{\perp}$, and the charge density, spin density, and orbital moment are all anisotropic. The polarized nature of X-rays allows one to quantitatively probe this anisotropy. The correlations between the measured angle-dependent white-line and dichroism intensities and the anisotropic charge and spin distribution in the Wigner–Seitz cell and the anisotropic orbital moment are expressed by three powerful sum rules [28–30] to be discussed below.

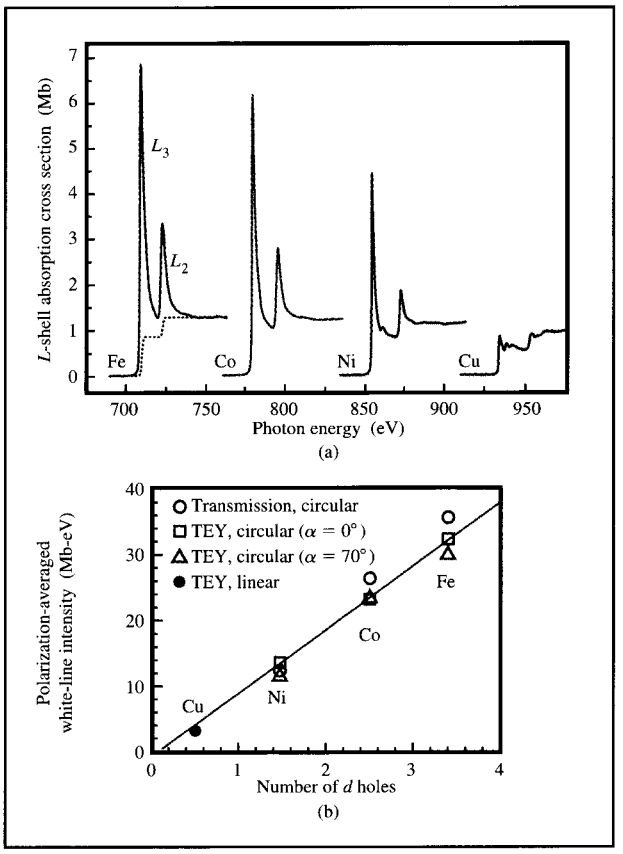

Figure 3

(a) L-edge X-ray absorption spectra for Fe, Co, Ni, and Cu metal. The Fe, Co, and Ni spectra were recorded in transmission [26], while the Cu spectrum was obtained with linearly polarized light by total electron yield detection [25]. We have plotted absolute cross sections which were obtained by fitting the experimental spectra to known cross sections [27] below and above the L edges. (b) White-line intensity, determined after subtraction of a double step function [26], shown dashed in the Fe spectrum in (a), versus calculated d-orbital occupation [22, 23]. We have plotted data obtained by different detection methods and different X-ray incidence angles α, measured from the surface normal. The electron yield intensities have been corrected for saturation effects.

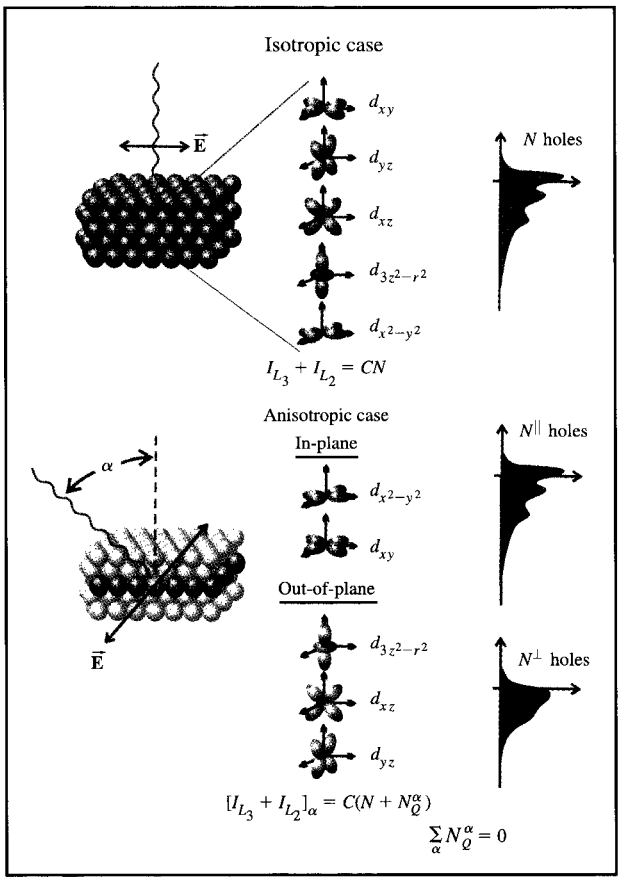

Figure 5

Illustration of the charge sum rules linking the white-line intensities to the number of d holes, N (isotropic case) and to N and the charge density, N_Q^α (anisotropic case). If the crystal symmetry is high, the states with different d-orbital symmetries contain an equal number of holes, and the charge density in the Wigner–Seitz cell is isotropic. In this case the measured white-line intensity $I_{L_3} + I_{L_2}$ is independent of the X-ray polarization, and it is directly proportional to N. The proportionality constant C is simply the square of the $p \rightarrow d$ radial transition matrix element. For a thin metal layer sandwiched between other layers, the bonding is anisotropic, and states with in-plane symmetry have a different number of d holes, $N^{\|}$, than states with out-of-plane symmetry, $N^{\perp}$, as shown in the bottom half of the figure. In this case the "searchlight" effect in X-ray absorption leads to a polarization-dependent white-line intensity, labeled by an angle α. The general charge-sum rule then relates the angle-dependent white-line intensity to N, as well as to the angle-dependent charge density N_Q^α, which is a linear combination of $N^{\|}$ and $N^{\perp}$. When averaged over different crystallographic directions, the charge density term vanishes ($\Sigma_\alpha N_Q^\alpha = 0$).

- *Charge sum rule*

The total intensity sum rule correlating the polarization-dependent white-line intensity with the charge distribution around the absorbing atom is illustrated in Figure 5. The basic principle underlying this sum rule is the so-called "searchlight" effect [31, 36]. Because X-ray absorption is governed by electric dipole transitions, the photoelectrons are preferentially excited in the direction of the electric field vector $\vec{\mathbf{E}}$. Thus, the $\vec{\mathbf{E}}$ vector can be envisioned as a "searchlight" revealing whether there are empty valence states in a given direction. In an isotropic bonding environment, the searchlight sees the same number of holes in all directions, and the white-line intensity is independent of the X-ray incidence angle on the sample. For this case we have the sum rule $I_{L_3} + I_{L_2} = CN$, where C is the square of the $p \rightarrow d$ radial transition matrix element. Figure 4(b) confirms the expected linear relationship between the white-line intensity and the calculated number of $3d$ holes [22, 23] for Fe, Co, Ni, and Cu.

In contrast, for a single metal layer sandwiched between two layers of a different metal, shown in Figure 5, the bonding is anisotropic. Now the white-line intensity depends on the X-ray incidence angle on the sample, α. The sum rule for this case may be written [30] as

$$[I_{L_3} + I_{L_2}]_\alpha = C(N + N_Q^\alpha), \tag{1}$$

where the factor N_Q^α can be expressed as a linear combination of $N^{\|}$ and $N^{\perp}$ [31] (see also Footnote 3); it depicts the anisotropy of the charge density in the unit cell. This term vanishes when an angular average is performed, $\Sigma_\alpha N_Q^\alpha = 0$, and the isotropic sum rule is obtained. The number of holes, N, represents, of course, a quantity integrated over the Wigner–Seitz cell, and it is isotropic by definition.

- *Spin sum rule*

For $3d$ transition metals the spin-orbit coupling is small, and charge and spin remain essentially decoupled. As a consequence, the spin sum rule [29], illustrated in **Figure 6**, may be expressed [30, 31] in the form of Equation (1),

$$[A - 2B]_\alpha = -\frac{C}{\mu_B}(m_s + m_D^\alpha). \tag{2}$$

The total number of holes N is simply replaced by the spin moment $m_s = (N^\uparrow - N^\downarrow)\,\mu_B$, and the charge density term N_Q^α is replaced by a spin density term $m_D^\alpha = 4[N_Q^{\alpha\uparrow} - N_Q^{\alpha\downarrow}]\,\mu_B$. The spin density term can also be called an intra-atomic magnetic dipole moment [29, 30]. It is nonzero in anisotropic bonding environments and reflects the fact that the number of spins in the unit cell differs along different crystallographic directions. The searchlight-like capability of polarized X-rays allows observation of this term. It is not observed in conventional magnetization measurements, which probe only the total, unit-cell-integrated, and therefore isotropic, spin moment m_s, but it can be detected in spectroscopies which sense

[3] Note that N_Q^α also differs for linear and plane-polarized X-rays.

the hyperfine field at the nucleus [37]. The term m_D^α vanishes when an angular average is performed, viz., $\Sigma_\alpha m_D^\alpha = 0$, and the isotropic sum rule is obtained [30]. The angular average requires that in all measurements the sample be magnetically saturated along the X-ray propagation direction (the photon spin direction of the circularly polarized light). In practice this requires that the measurements be performed in a sufficiently strong external magnetic field.

• *Orbital sum rule*

The origin of the orbital magnetic moment m_o and its anisotropy is illustrated in **Figure 7**. An orbital moment exists if there is a net orbital current from the motion of the d electrons around the nucleus, causing an imbalance of states with quantum numbers $m_l = +1, +2$ and $m_l = -1, -2$, as shown in Figure 2. This requires time-reversal symmetry to be broken. In magnetic materials the symmetry breaking is caused by the spin-orbit coupling, which leads to a clockwise/counterclockwise imbalance of orbital electron motion in the plane perpendicular to the spin moment.

The electronic states created by the crystal potential alone possess no orbital moment, since all d orbitals have a perfect balance of $\pm m_l$ contributions [31]. This balance is broken by the spin-orbit interaction, which mixes different d orbitals to produce a nonzero angular momentum [31, 38]. If the bonding environment is highly symmetric (e.g., cubic), the orbital moment has the same magnitude, independent of the sample magnetization direction, as shown in Figure 7. If the bonding is anisotropic, however, the d electron (charge) orbits are anisotropic. When the sample is magnetized in different directions, i.e., by rotating the spin moment by a sufficiently strong external magnetic field, an orbital moment arises from the clockwise/counterclockwise imbalance of orbital motion in the plane perpendicular to the spin quantization axis as a consequence of the spin-orbit coupling. Because of the anisotropic charge cloud, the orbital amplitudes differ for different magnetization (spin moment) directions, and the orbital moment is anisotropic. For example, if the charge distribution is pancake-like and in-plane, as shown in Figure 7, the out-of-plane orbital moment is larger than the in-plane one, in agreement with the intuitive picture that the in-plane electron or hole current should have a larger average radius than its out-of-plane counterpart. The direction of the orbital moment relative to the spin moment is given by Hund's rule. For a more (less) than half-filled d shell, m_o and m_s have the same (opposite) sign, i.e., are parallel (antiparallel).

XMCD directly measures the component of the orbital moment along the photon spin direction, since the X-ray helicity couples directly to the orbital electron motion. In the presence of an external magnetic field which is sufficiently large to magnetically saturate the sample, the orbital moment m_o^α along the field direction α can be determined directly by use of the sum rule [28]

$$[A + B]_\alpha = -\frac{3C}{2\mu_B} m_o^\alpha . \qquad (3)$$

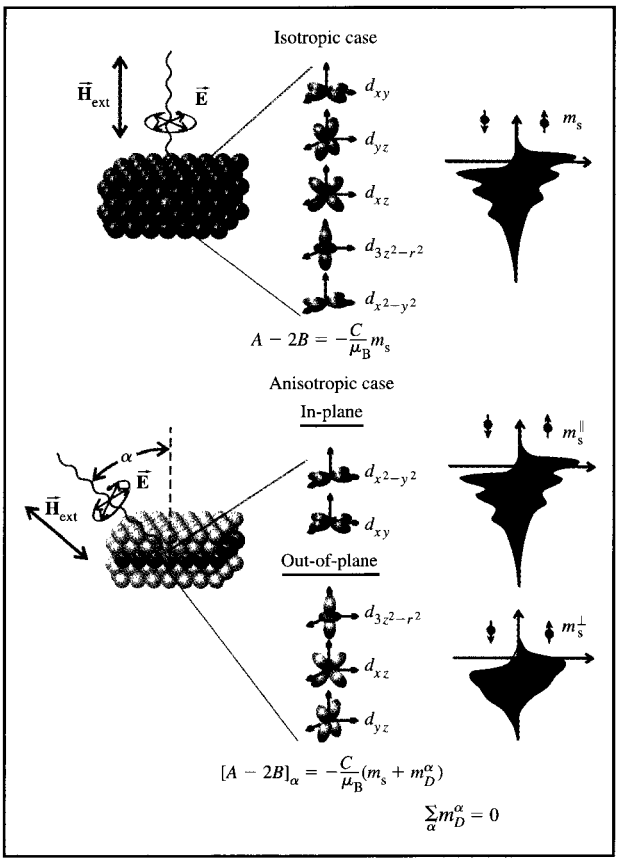

Figure 6

Illustration of the spin rules linking the dichroism intensities to the spin moment m_s of the d shell (isotropic case) and to m_s and the spin density m_D^α (anisotropic case). If the crystal symmetry is high, the states with different d-orbital symmetries have the same spin moment, and the spin density in the Wigner–Seitz cell is isotropic. In this case the measured dichroism intensity $A - 2B$ is independent of the X-ray incidence angle and is directly proportional to m_s. The proportionality constant C is the square of the $p \rightarrow d$ radial transition matrix element, as in the charge case. For a thin metal layer sandwiched between other layers, the bonding is anisotropic, and states with in-plane symmetry have a different spin moment contribution $m_s^{\parallel}$ than states with out-of-plane symmetry $m_s^{\perp}$, as shown in the bottom half of the figure. Note that the total moment, $m_s = 2m_s^{\parallel} + 3m_s^{\perp}$, is isotropic by definition. The general spin sum rule relates the angle-dependent dichroism intensity to m_s and to an angle-dependent spin density m_D^α, which is a linear combination of $m_s^{\parallel}$ and $m_s^{\perp}$. When averaged over different crystallographic directions, the spin density term vanishes ($\Sigma_\alpha m_D^\alpha = 0$).

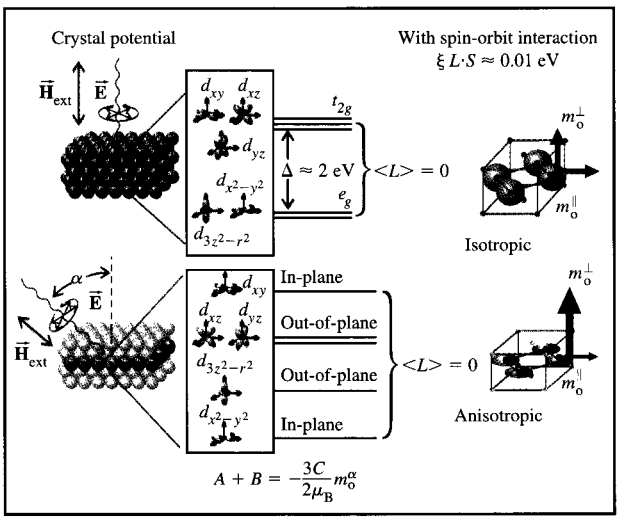

Figure 7

Origin of the orbital magnetic moment and the orbital sum rule, illustrated via a *d*-orbital-based bonding model. The crystal potential gives rise to a splitting of the *d* orbitals which reflects the symmetry of the lattice. For cubic symmetry, for example, states of t_{2g} and e_g symmetry are split by an energy $\Delta \approx 2$ eV. The pure *d* orbitals possess no orbital moment, since contributions from $m_l = +1, +2$ states cancel those from $m_l = -1, -2$ states [31]. This balance is destroyed by the spin-orbit interaction, which leads to new states with unequal $\pm m_l$ contributions. If the crystal symmetry is high, the *d*-orbital bonding is isotropic, and the size of the orbital moment is independent of the magnetization direction, as shown in the top part of the figure. If the bonding is anisotropic, as in the case of a multilayer, shown in the bottom part of the figure, the splitting between the in-plane and out-of-plane *d* orbitals is different. In the presence of spin-orbital coupling, the resulting orbital moment is anisotropic. Since the X-ray helicity couples directly to the orbital electron motion, XMCD measures the component of the orbital moment m_o^{α} along the photon spin direction α. This is expressed by the orbital sum rule stated in the figure.

It is interesting to note that one would expect a correlation among the anisotropy of the orbital moment m_o^{α}, the charge density N_Q^{α}, and the spin density m_D^{α}, since all three originate from crystallographic anisotropies. Calculations for a Co monolayer show, however, that the anisotropy of the charge term is considerably smaller than that of the magnetic terms [31, 39]. The expected correlation among the magnetic anisotropy terms is in fact observed, as discussed in the section on the anisotropy of magnetic moments.

- *Magic geometries*

As discussed above, the quantities N_Q^{α}, m_D^{α}, and m_o^{α} all depend on the measurement geometry, characterized by α. In practice, it is convenient to limit the number of angle-dependent measurements. For multilayers with uniaxial geometry about the surface normal, two "magic" geometries are particularly useful. The first one, suggested by Stöhr and König [30], makes it possible to determine the angle-averaged quantities N, m_s, and $m_o = (m^{\perp} + 2m^{\parallel})/3$ in a single measurement. Assuming circularly polarized light, it consists of a measurement with the photon spin and the external magnetic field (strong enough to saturate the sample), oriented at the "magic" angle $\alpha = 54.7°$ from the surface normal. The second one, due to Dürr and van der Laan [40], makes it possible to determine the size of the anisotropic magnetic terms $m_D^{\perp} - m_D^{\parallel}$ and $m_o^{\perp} - m_o^{\parallel}$. It consists of a "forbidden geometry" measurement for which the photon spin is *perpendicular* to the external magnetic field (strong enough to saturate the sample), and the sample is at $\alpha = 45°$ X-ray incidence.

5. Test of sum rules

The sum rules link the white-line or XMCD intensity to an electronic or magnetic ground-state property. In all cases the two quantities are linked by a proportionality constant C, which is the square of the transition matrix element. One can test the relative validity of the various sum rules by comparing values of C determined from experimental intensities I_{L_3}, I_{L_2}, A, and B in conjunction with the most reliable literature values of N, m_s, and m_o. This is illustrated in **Figure 8** using XMCD transmission data by Chen et al. for Fe, Co, and Ni [26] and theoretical [22, 23] and gyromagnetic ratio [41] values for N, m_s, and m_o. We have neglected all anisotropy effects, which for the highly symmetric bulk metals should be a good assumption. In all cases, the constant C is found to have a value close to 10 Mb-eV. Unfortunately and surprisingly, the values for N, m_s, and m_o are only known with a precision of a few percent. It is therefore not clear whether the variations in Figure 8 are due to limitations in the sum rule or uncertainties in the literature values for N, m_s, and m_o. Nevertheless, it appears that the sum rules have a reliability of at least 10% for absolute moment determinations and even more for moment determinations relative to a standard, measured under the same experimental conditions. The sum rules have also been tested by means of electronic structure calculations by Wu and Freeman [42, 43]. These authors also obtained a reliability of about 10% but found it necessary to cut off the energy integration 6 eV above the Fermi level. This is contrary to the experimental requirement of extending the integrals well above the edge to obtain convergence [26].

6. Experimental details and data analysis

The XMCD measurements, reported below, were performed at room temperature at the Stanford Synchrotron Radiation Laboratory on its "8–2" beam line. Circularly (~90 ± 5%) polarized light was obtained by

moving a vertically deflecting mirror below the electron orbit plane of the storage ring. In the studies reported below, the sample was centered in the 5-cm gap of an electromagnet which could be ramped to more than 90% of full field within one second. XMCD measurements were recorded in a 10-kOe external magnetic field parallel to the X-ray propagation direction, at variable angles α with respect to the surface normal. X-ray absorption was measured using right-circularly-polarized X-rays and switching the magnetization direction parallel and then antiparallel to the photon spin at each photon energy step. Measurements on samples made in the form of wedges were performed as a function of wedge thickness by translating the sample along the wedge direction. The X-ray beam spot size was about 1 mm horizontally and 0.75 mm along the vertical translation direction, ensuring adequate spatial resolution.

In quantitative XMCD studies, extreme care must be exercised in the accurate determination of the measured intensities. The orbital moment determination is especially difficult because the sum-rule intensity is the difference of two large intensities. Unfortunately, the most reliable transmission technique cannot be generally used because of the problems associated with making samples of interest in the form of free-standing films, which in the soft-X-ray region would have to be less than 1000 Å thick to avoid saturation effects. Such measurements have recently been carried out, however, by Chen et al. [26] for Fe, Co, and Ni metal films, and we have used these data above to test the sum rules.

There are two other possible detection schemes—fluorescence and electron yield detection. Fluorescence yield measurements typically suffer from saturation effects for all but highly diluted samples [44], and experimental studies suggest that the fluorescence yield may not quantitatively follow the true absorption dichroism signal [45], despite theoretical predictions [46] to the contrary. Electron yield measurements may also suffer from saturation effects [20], and the switching of the external magnetic fields during measurement may cause problems in reliably normalizing the data for the two field orientations relative to each other. Nevertheless, these problems can be overcome as discussed below, and electron yield detection is the technique of choice for soft-X-ray absorption and XMCD measurements.

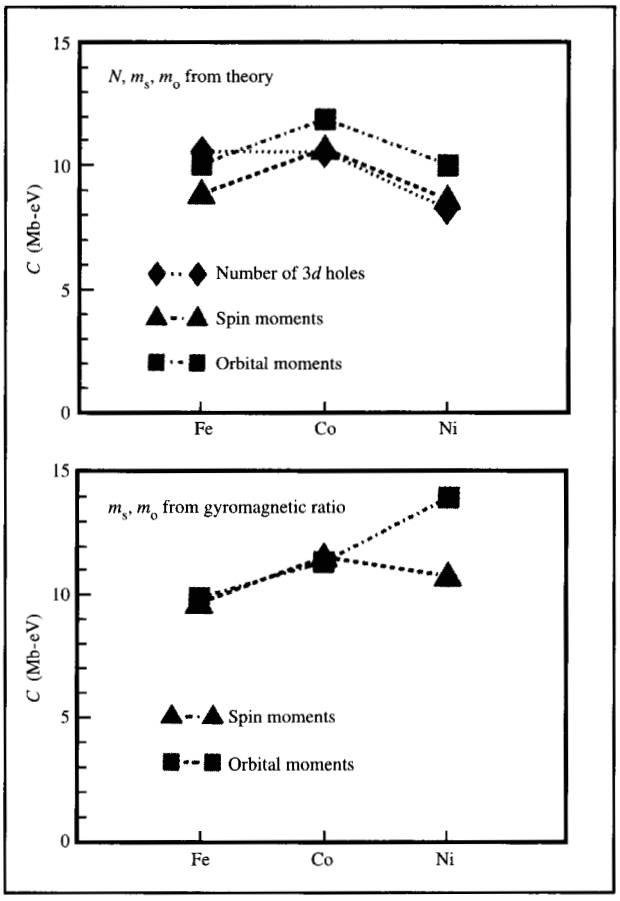

Figure 8

Test of sum rules using XMCD transmission data by Chen et al. [26] for Fe, Co, and Ni and values for N, m_s, and m_o from theory [22, 23] or from gyromagnetic ratio data [41]. Plotted is the square of the radial transition matrix element C obtained from the sum rules [Equations (1), (2), and (3)], neglecting anisotropy effects.

• *Electron yield measurements*

Figure 9 shows how the electron yield in the presence of magnetic fields is measured. The experimental arrangement shown in the figure is aimed at the measurement of "real" samples, made *ex situ*. In order to protect the samples from degradation, they always contain a capping layer of Au or Pt, typically 15–20 Å in thickness. The ultrahigh vacuum of the electron storage ring and the beam line are decoupled from the vacuum of the sample chamber (typically 10^{-6} torr) by a differential pumping section. The incident photon flux is monitored by a Au grid reference monitor, which, like the sample, is placed inside a cylindrical tungsten cage as shown. Both cages are kept at a positive bias voltage to collect the photoelectrons, and in the presence of large magnetic fields they are also found to minimize asymmetries in the direct photocurrent of the sample and reference grid [31].

• *Data analysis*

Data analysis starts with the division of the electron yield signal from the sample by that from the reference monitor. A linear background is then fitted to the pre-edge region and subtracted from the two spectra obtained

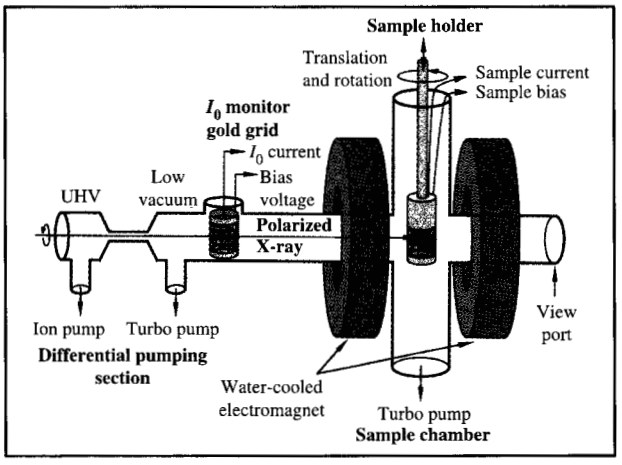

Figure 9

Experimental arrangement for high-field XMCD measurements. A differential pumping section decouples the ultrahigh vacuum of the monochromator from the high vacuum ($\sim 10^{-6}$ torr) of the sample chamber (aluminum-walled). The intensity of the circularly polarized X-ray beam is first monitored by a gold grid reference monitor (~80% transmission) surrounded by a cylindrical tungsten cage (92% transmission). A similar cage also surrounds the sample, which is located in the 5-cm gap of a split-coil electromagnet. The X-rays enter the sample chamber through one of the pole shoes of the magnet, parallel to the magnetic field. The cages are kept at a positive bias voltage and the photocurrents from the Au grid and the sample are measured with a current amplifier.

for opposite fields. Quantitative XMCD intensities suited for sum-rule analysis may be obtained by two procedures.

The first procedure relies on the use of a reference sample with known magnetic properties. In this case both the standard and the unknown, preferably consisting of the same element, are treated identically in the measurement and analysis phases. After normalization and background subtraction, the spectra are normalized to the same edge jump, arbitrarily set to unity, in the energy range 60–100 eV above the L_3 edge. This ensures that the measured dichroism signal is normalized to the same number of atoms in the sample [36]. The XMCD intensities are obtained by taking the difference of the two spectra recorded with opposite polarization or magnetization directions; by direct comparison of the spin and orbital sum-rule intensities for the standard and the "unknown," the moments for the unknown are determined. This procedure implicitly assumes transferability of the proportionality constant C between different samples, and thus assumes that the radial transition matrix element is insensitive to bonding effects.

The second method uses the charge sum rule in conjunction with the other two magnetic sum rules and does not require a reference sample. Here one assumes that, for a given sample, the constant C is identical for the three sum rules, as predicted by atomic-like theory which ignores any energy dependence of the transition matrix element across the d band and s–d hybridization effects. As discussed by Wu and Freeman [42, 43], this may not be exactly correct when the finite extent of nearest-neighbor bonding (band structure) is taken into account. In this case the data do not have to be normalized to the same edge jump, since the white-line intensity is itself proportional to the number of sampled atoms. Hence, one can directly determine the white-line intensity from the sum of the spectra, and the dichroism intensity from the difference of the spectra. By combining the charge sum rule with either magnetic sum rule, the constant C is eliminated and the ratio of XMCD sum-rule intensity to white-line intensity is directly related to the ratio of magnetic moment to number of holes. Since in transition-metal films the number of holes for a given element varies much less than the magnetic moment, one can assume the elemental bulk value for the number of holes (see Figure 2) in the sample under study, and can therefore determine its magnetic moments.

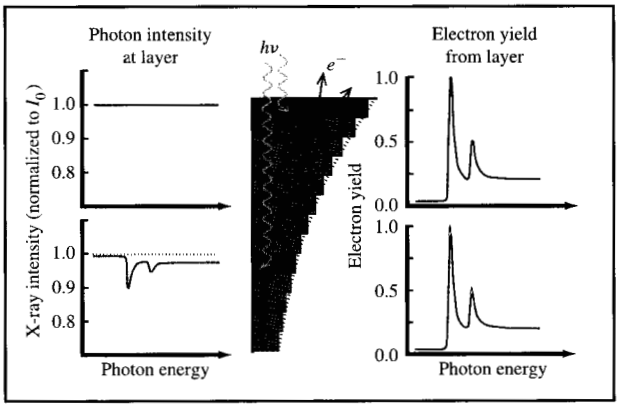

Figure 10

Illustration of the origin of saturation effects in electron yield detection, using the L-edge spectrum of Fe as an example. The electron yield contributions from the various layers of the samples decay with a $1/e$ length of about 17 Å, as shown. The X-rays incident on the first layer have an intensity which is energy-independent, as shown on the left, and an electron yield signal which follows the X-ray absorption cross section, as shown on the right. The photon intensity at layers deeper in the sample exhibits an energy-dependent structure which is characteristic of the X-ray absorption in the outer layers and therefore inversely follows the X-ray absorption cross section. The electron yield from a layer within the sample is therefore convoluted with the modulated X-ray intensity incident on the layer. The signal from the layer shows a reduced or saturated intensity at the L_3 and L_2 edges, as illustrated on the right for a layer that is 17 Å below the surface, assuming normal X-ray incidence.

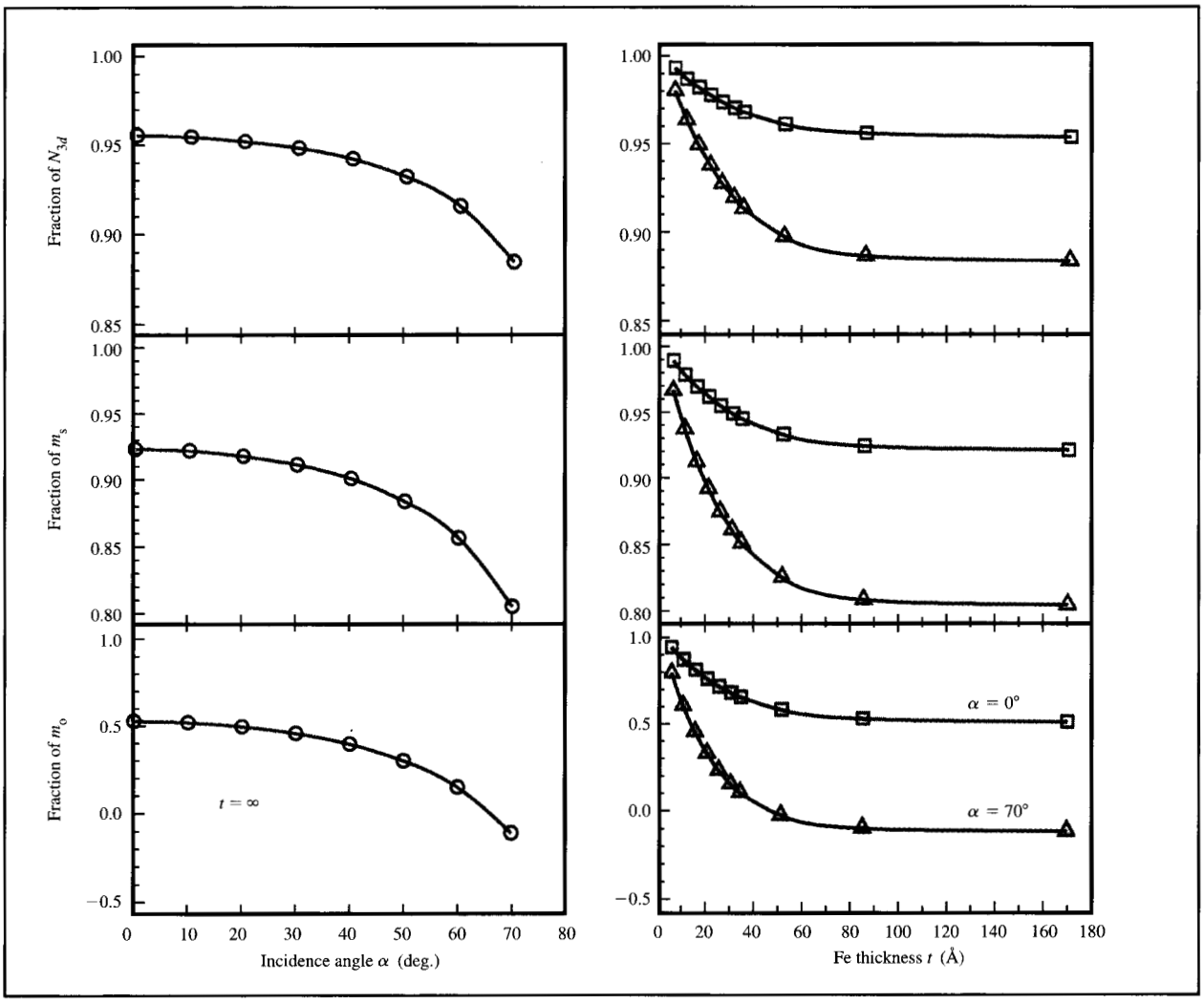

Figure 11

Saturation effects in electron yield detection for L-edge spectra of Fe, calculated from the transmission cross section plotted in Figure 4(a) and assuming an electron sampling depth of 17 Å. In all cases we have plotted the quantity (sum-rule intensity)/(edge jump) calculated for total electron yield detection divided by (sum-rule intensity)/(edge jump) measured in transmission. According to the first analysis procedure discussed in the data analysis section, the plotted quantities correspond to the fraction of the "true" (i.e., transmission) values for N, m_s, and m_o that would be obtained if total electron yield detection were used. The angle α is measured from the surface normal.

• *Correction of saturation effects*

Saturation effects arise when the X-ray absorption depth in the sample becomes comparable to the electron yield (or fluorescence yield) sampling depth, as illustrated in **Figure 10**. We have measured the total electron yield sampling depth in Fe, Co, and Ni metals and obtained the values 17 Å (Fe), 25 Å (Co), and 25 Å (Ni). The $(1/e)$ X-ray absorption length λ_x in the L-edge region is, of course, strongly energy-dependent, since it is inversely proportional to the absolute X-ray absorption cross section, plotted in Figure 4. For example, for Fe we obtained λ_x = 165 Å at the L_3 peak, λ_x = 325 Å at the L_2 peak, and λ_x = 800 Å above the edges (750 eV). With knowledge of these numbers, it is then straightforward to correct for saturation effects. The reduction factors for the quantities N, m_s, and m_o obtained from total electron yield relative to transmission data are plotted in **Figure 11** for bulk Fe as a function of X-ray incidence angle α, and for two incidence angles as a function of Fe thickness. Saturation effects were found to be relatively small for the white-line and spin-moment intensities but large for the orbital moment. Because of the smaller L_3 white-line cross

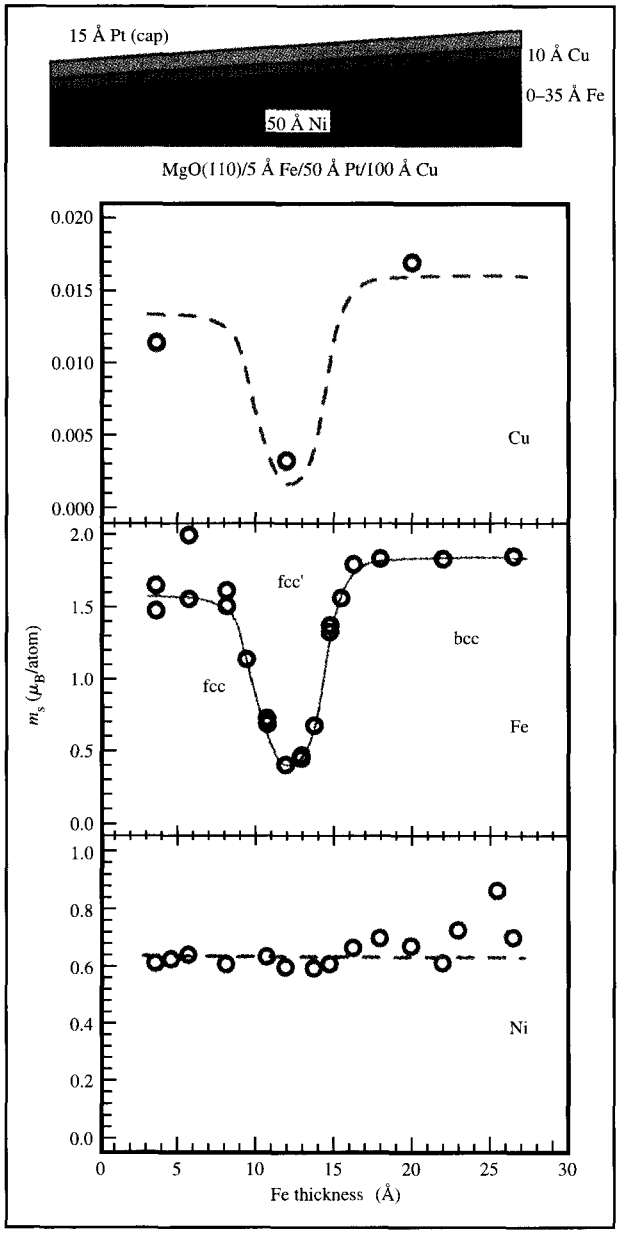

Figure 12

Element-specific magnetic spin moments determined by XMCD sum-rule analysis in a Ni/Fe/Cu wedge, shown at the top, as a function of Fe thickness. The Fe moment was found to be strongly thickness-dependent, which is attributed to a changing crystallographic structure in the Fe film, as indicated. The Cu layer acquires a weak induced magnetic moment which follows that of Fe. The Ni substrate layer was found to have a nearly constant bulk-like magnetic moment.

sections [Figure 4(a)], saturation effects are smaller in Co and Ni than in Fe.

7. Applications

• *Determination of element-specific moments*

One of the parts of Figure 1 pertains to the use of the spin-valve head to read the bits on a magnetic recording disk. In practice, spin-valve heads have a more complicated structure than shown [9]. As discussed by Parkin [47], the GMR effect or sensor signal is considerably enhanced without a significant change in coercivity by insertion of Co nanolayers at the interfaces of a conventional $Ni_{80}Fe_{20}$/Cu/$Ni_{80}Fe_{20}$ spin valve [8]. In such structures the GMR response increases by more than a factor of 2 when the Co nanolayer thickness exceeds about 10 Å. The enhanced GMR response in such $Ni_{80}Fe_{20}$/Co/Cu/Co/$Ni_{80}Fe_{20}$ structures is attributed to enhanced spin-dependent scattering in the Co nanolayers. One may expect a similar or even greater enhancement of the GMR response when Fe is used instead of Co because of the larger magnetic moment of Fe. Experiments similar to those described by Parkin [47], however, have shown a complicated GMR response, in particular a pronounced minimum at an Fe thickness near 12 Å, where the GMR effect was close to zero.[4]

XMCD magnetometry is ideally suited to investigate the origin of this effect, since the magnetic moments in the individual layers can be separately obtained. We have investigated the GMR breakdown in a Ni/Fe/Cu/Fe/Ni nanolayered spin valve. For experimental convenience we used a model structure consisting of half a spin valve, grown by dc magnetron sputtering as a Ni(50 Å)/Fe(0–35 Å)/Cu(10 Å) wedge with a 15-Å-thick Pt cap on top of a MgO(110)/Fe(5 Å)/Pt(50 Å)/Cu(100 Å) template, as shown in **Figure 12**. The element-specific spin moments, obtained by sum-rule analysis, are also shown in the figure. The measurements were carried out at a 60° incidence angle, close to the 54.7° "magic" angle, so that the magnetic dipole term could be neglected in the analysis. The moments were derived by using a combination of the isotropic charge and spin sum rules (second method in the section on data analysis) and assuming bulk values for the number of d holes (see Figure 4). While the Ni spin moment was nearly constant, with a value close to that of bulk Ni (0.64 μ_B), the Fe moment displayed a dramatic decrease at a thickness near 12 Å. The larger scatter in the determined Fe moments at small Fe thickness was caused by the reduced Fe signal. Similarly, the Ni moments at large Fe thickness displayed more scatter because the electron yield signal from Ni was attenuated by the Fe layer. The average Cu moment follows that of Fe, since it originates from the induced moment in Cu interface atoms through hybridization of the Fe and Cu d bands [48, 49]. Extended X-ray

[4] S. S. P. Parkin, private communication, 1996.

absorption fine-structure measurements[5] have shown that the changes in the Fe moment result from a change in crystallographic structure, as indicated in Figure 12. When the Fe layer is thin, its structure follows that of the fcc Ni template, while it assumes the bulk Fe bcc structure above a thickness of about 17 Å. Similar structural effects have been observed in sputtered Fe/Cu multilayers [25, 50], and similar magnetic effects have been observed for Fe on Ni(100) [21].

The above results demonstrate the power of XMCD to reveal the magnetic contributions of different layers in complex magnetic structures. In particular, they demonstrate the delicate interplay between crystallographic and magnetic properties in thin films. The observed decrease in the spin-valve GMR in nanolayered Fe structures is attributed to magnetically "dead" Fe which is either in an antiferromagnetic or nonmagnetic phase.

• *Anisotropy of magnetic moments*

The microscopic origin of magnetic anisotropy in transition metals has been debated for more than 60 years, dating back to early work by Van Vleck [51]. Recently, interest in this problem has been revived in conjunction with artificially created transition-metal films and multilayers which exhibit perpendicular magnetic anisotropy (PMA) [2, 3]. It is clear that PMA is due to an intrinsic, i.e., magnetocrystalline, anisotropy mechanism strong enough to overcome the extrinsic macroscopic shape anisotropy, which favors an in-plane orientation of the magnetization [38], as illustrated in **Figure 13**. The in-plane preference of the shape anisotropy in a thin-film sample arises from the fact that the dipole–dipole interaction between the atomic magnetic moments in the sample is minimized if the moments align themselves parallel to the largest spatial extent of the sample, which is in-plane. For layered materials, the PMA has been attributed to symmetry breaking at the interfaces in conjunction with spin-orbit coupling. The microscopic details have remained fuzzy, however. In the following we take a closer look at the microscopic origin of the magnetocrystalline anisotropy and how it leads to PMA.

As a model structure we have investigated a Au/Co/Au sample, shown schematically in Figure 14, consisting of ten Co terraces of 2 mm width and thicknesses between 3 and 12 atomic layers (AL) of Co sandwiched between a 28-nm-thick (111) Au buffer, grown onto a float-glass substrate, and an ~9-AL-thick Au capping layer. The sample exhibited a transition from in-plane anisotropy at large Co thickness to out-of-plane behavior at $t_{Co} \leq 11$ AL [52, 53].

Figure 14 shows the results of an orbital sum-rule analysis of XMCD data obtained for two sample

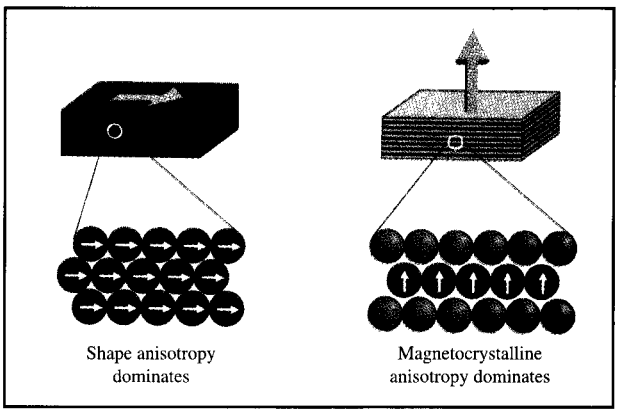

Figure 13

Illustration of two anisotropy mechanisms which determine the easy magnetization axis in thin films and multilayers. The shape anisotropy arises from the dipolar coupling of atomic moments and favors alignment of the moments along the largest extent of the sample, i.e., parallel to the film (a macroscopic spin–spin dipolar anisotropy). The magnetocrystalline anisotropy is determined by the microscopic bonding in the sample. In multilayer systems, the anisotropic bonding environment at or near interfaces may lead to a preferred perpendicular alignment of the magnetization, as covered in more detail in Figure 14.

orientations as a function of Co thickness. The actual in-plane component $m_o^{\parallel}$ was derived from the experimental data taken at angles $\alpha = 65°$ and $\alpha = 0°$ by assuming uniaxial anisotropy such that $m_o^{\alpha} = m_o^{\perp} \cos^2 \alpha + m_o^{\parallel} \sin^2 \alpha$. The orbital moment was found to be strongly anisotropic, with a value $\Delta m_o = m_o^{\perp} - m_o^{\parallel}$ up to ~0.15 μ_B at the 4-AL Co step. The difference Δm_o decayed rapidly with a $1/t_{Co}$ behavior and became smaller than the experimental error for thicknesses larger than 7 AL. The angle-averaged orbital moment $(m_o^{\perp} + 2m_o^{\parallel})/3$ remained essentially constant at the Co bulk value of $m_o = 0.14$ μ_B.

As discussed elsewhere [31, 53], the spin moment was also found to be thickness-independent, while the anisotropy in the dipole moment was found to track that of the orbital moment, with values $m_D^{\parallel} = -0.112$ μ_B and $m_D^{\perp} = 0.224$ μ_B at 4-AL thickness. This underscores the close relationship between orbital and dipolar anisotropies mentioned earlier.

The importance of these results is that they provide experimental support for a simple model of the microscopic origin of the magnetocrystalline anisotropy [38, 54], as illustrated in Figure 14. At the thick end of the wedge, the orbital magnetic moment is nearly isotropic. The in-plane magnetic anisotropy of the sample arises simply from the macroscopic shape anisotropy. Because it is due to the dipolar coupling of atomic moments and because the size of the total atomic moment

[5] S. Conradson, private communication, 1996.

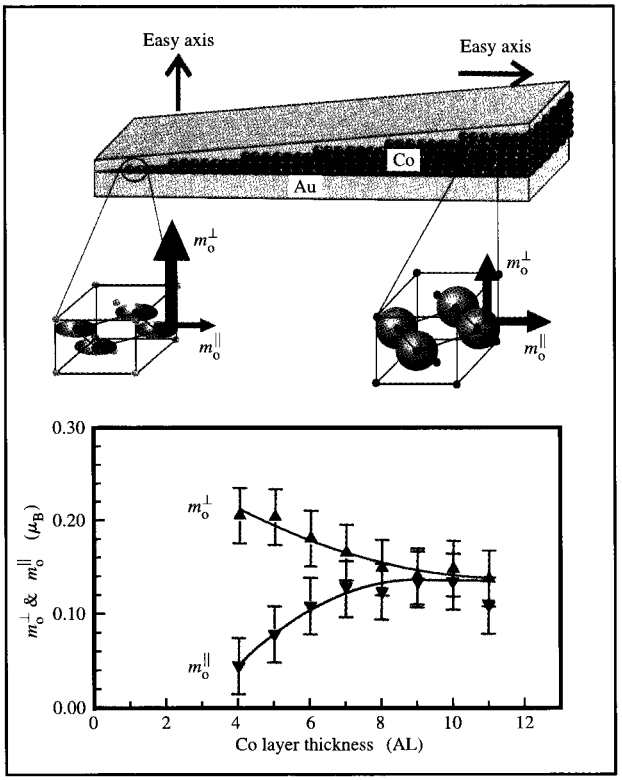

Figure 14

Origin of the magnetocrystalline anisotropy, illustrated by XMCD results for a Au/Co/Au wedge sample [53, 67]. The wedge shown had an in-plane easy axis at its thick end and an out-of-plane easy axis at its thin end. The measured angle-dependent orbital moments, $m_o^\perp$ and $m_o^\parallel$, as a function of Co thickness were found to become increasingly anisotropic, with a considerably larger perpendicular orbital moment at the thin end. The measurements show that the anisotropy of the orbital moment is the microscopic origin of the magnetocrystalline anisotropy.

is dominated by the spin moment, one may regard the shape anisotropy as a macroscopic spin–spin dipolar anisotropy. With decreasing sample thickness, the average symmetry of the Co atoms becomes increasingly anisotropic. At the thin end of the wedge the anisotropy of the orbital moment has become so large that it has a strong preference for a perpendicular orientation. Now there are two opposing forces acting on the spin moment. The presence of the dipolar field favors in-plane rotation, whereas the presence of the spin-orbit coupling favors rotation parallel to the out-of-plane orbital moment (Hund's rule). The easy axis is determined by which of the two forces is stronger, i.e., whether the dipolar energy is smaller or larger than the anisotropy of the spin-orbit energy. Clearly, at the thin edge of the wedge the anisotropy energy associated with the orbital moment exceeds the value of the shape anisotropy, and we have the interesting situation that the small orbital moment redirects the larger spin moment into a perpendicular alignment.

The case of perpendicular magnetic anisotropy is of considerable interest for technological applications. As discussed elsewhere [31, 55], it may be implemented by sandwiching a thin magnetic layer between other layers that "bond strongly" to it, as in a Au/Co/Au sandwich. Our results therefore also indicate how to obtain multilayers with large perpendicular anisotropy.

8. Conclusions

In this overview, we have described the basic principles and techniques of quantitative XMCD spectroscopy and have presented two examples of the use of the technique for the determination of element-specific spin and orbital magnetic moments. It is clear that XMCD has already been used to address important issues in magnetism that are difficult or impossible to examine with conventional techniques. There are many other capabilities and applications of XMCD which have not been covered here for reasons of space constraints; for completeness, we close this paper by mentioning a few.

XMCD is not only element-specific but even offers chemical specificity, as demonstrated by Sette et al. in studies of spinels and garnets [17]. In thin transition-metal films the presence of an oxide component, for example, is readily detected by an L_3 peak which is chemically shifted to higher binding energy. The element-specific nature of XMCD can be used to measure element-specific hysteresis loops of heteromagnetic systems [56]. The magnetic contributions of different electronic valence subshells can be probed by selection of appropriate core shells. For example, for the Co/Cu system both the L-shell [48] and K-shell [57] XMCD spectra have been measured, revealing the magnetic contributions of the p and d valence electrons, respectively. The induced moments in $5d$ metal atoms have been studied by L-edge XMCD [58–60], and the $M_{2,3}$-edge has been used to obtain the induced magnetic moment of the $4d$ transition metal Rh [61]. The temperature dependence of the magnetization in thin films on surfaces has been investigated down to monolayer coverage [19–21, 62, 63]. Also noteworthy is the use of XMCD in conjunction with a small oscillating external magnetic field to obtain the element-specific ac susceptibility [64], which yields information not only about the magnetic properties of the films, but also about their structural properties. Finally, since the XMCD intensity varies with the cosine of the angle between the photon spin and the magnetization direction, it can be used to determine the easy magnetization direction in thin films

[65] and can be used for magnetic imaging [18, 66], offering elemental specificity as well as the capability to investigate buried layers.

Acknowledgment

This work was carried out in part at Stanford Synchrotron Radiation Laboratory, which is operated by the Department of Energy, Division of Chemical Sciences. We would like to thank our collaborators who were involved in the original work reviewed here, especially Mahesh Samant, Dieter Weller, Harald König, and Stuart Parkin. We are grateful to Yves Idzerda for providing XMCD transmission data for Fe, Co, and Ni.

References and notes

1. A. J. Freeman and R. Wu, *J. Magn. Magn. Mater.* **100,** 497 (1991).
2. U. Gradmann and J. Müller, *Phys. Stat. Sol.* **27,** 313 (1968).
3. P. F. Carcia, A. D. Meinhaldt, and A. Suna, *Appl. Phys. Lett.* **47,** 178 (1985).
4. M. N. Baibich, J. M. Broto, A. Fert, F. Nguyen Van Dau, F. Petroff, P. Eitenne, G. Creuzet, A. Friederich, and J. Chazelas, *Phys. Rev. Lett.* **61,** 2472 (1988).
5. G. Binasch, P. Grünberg, F. Saurenbach, and W. Zinn, *Phys. Rev. B* **39,** 4828 (1989).
6. S. S. P. Parkin, N. More, and K. P. Roche, *Phys. Rev. Lett.* **64,** 2304 (1990).
7. J. E. Hurst, Jr. and W. J. Kozlovsky, *Jpn. J. Appl. Phys.* **32,** 5301 (1993).
8. B. Dieny, V. S. Speriosu, S. S. P. Parkin, B. A. Gurney, D. R. Wilhoit, and D. Mauri, *Phys. Rev. B* **43,** 1279 (1991).
9. C. Tsang, R. E. Fontana, Jr., T. Lin, D. E. Heim, V. S. Speriosu, B. A. Gurney, and M. L. Williams, *IEEE Trans. Magn.* **30,** 3801 (1994).
10. J. M. Daughton, *Thin Solid Films* **216,** 162 (1992).
11. D. Tang, P. K. Wang, V. S. Speriosu, S. Le, and K. K. Kung, *IEEE Trans. Magn.* **31,** 3206 (1995).
12. J. S. Moodera, L. R. Kinder, T. M. Wong, and R. Meservey, *Phys. Rev. Lett.* **74,** 3273 (1995).
13. J. L. Erskine and E. A. Stern, *Phys. Rev. B* **12,** 5016 (1975).
14. G. Schütz, W. Wagner, W. Wilhelm, P. Kienle, R. Zeller, R. Frahm, and G. Materlik, *Phys. Rev. Lett.* **58,** 737 (1987).
15. G. Schütz, R. Frahm, P. Mautner, R. Wienke, W. Wagner, W. Wilhelm, and P. Kienle, *Phys. Rev. Lett.* **62,** 2620 (1989).
16. B. D. Cullity, *Introduction to Magnetic Materials*, Addison-Wesley Publishing Co., Inc., Reading, MA, 1972.
17. F. Sette, C. T. Chen, Y. Ma, S. Modesti, and N. V. Smith, in *X-Ray Absorption Fine Structure*, S. S. Hasnain, Ed., Ellis Horwood Limited, Chichester, England, 1991, p. 96.
18. J. Stöhr, Y. Wu, B. D. Hermsmeier, M. G. Samant, G. R. Harp, S. Koranda, D. Dunham, and B. P. Tonner, *Science* **259,** 658 (1993).
19. L. H. Tjeng, Y. U. Idzerda, P. Rudolf, F. Sette, and C. T. Chen, *J. Magn. Magn. Mater.* **109,** 288 (1992).
20. J. Hunter Dunn, D. Arvanitis, N. Mårtensson, M. Tischer, F. May, M. Russo, and K. Baberschke, *J. Phys.: Condens. Matter* **7,** 1111 (1995).
21. W. L. O'Brien and B. P. Tonner, *Phys. Rev. B* **52,** 1 (1995).
22. O. Eriksson, B. Johansson, R. C. Albers, A. M. Boring, and M. S. S. Brooks, *Phys. Rev. B* **42,** 2707 (1990).
23. P. Söderlind, O. Eriksson, B. Johansson, R. C. Albers, and A. M. Boring, *Phys. Rev. B* **45,** 12,911 (1992).
24. J. Stöhr and Y. Wu, in *New Directions in Research with Third-Generation Soft X-Ray Synchrotron Radiation Sources*, A. S. Schlachter and F. J. Wuilleumier, Eds., Kluwer Academic Publishers, Netherlands, 1994, p. 221.
25. H. Ebert, J. Stöhr, S. S. P. Parkin, M. Samant, and A. Nilsson, *Phys. Rev. B* **53,** 16,067 (1996).
26. C. T. Chen, Y. U. Idzerda, H.-J. Lin, N. V. Smith, G. Meigs, G. H. Ho, E. Pellegrin, and F. Sette, *Phys. Rev. Lett.* **75,** 152 (1995). Unpublished XMCD data for Ni have been graciously provided by Yves Idzerda.
27. B. L. Henke, E. M. Gullikson, and J. C. Davis, *At. Data Nucl. Data Tables* **54,** 181 (1993).
28. B. T. Thole, P. Carra, F. Sette, and G. van der Laan, *Phys. Rev. Lett.* **68,** 1943 (1992).
29. P. Carra, B. T. Thole, M. Altarelli, and X. Wang, *Phys. Rev. Lett.* **70,** 694 (1993).
30. J. Stöhr and H. König, *Phys. Rev. Lett.* **75,** 3748 (1995).
31. J. Stöhr, *J. Electron Spectrosc. Rel. Phenom.* **75,** 253 (1995).
32. The angular momentum of a photoelectron can be directly observed in a photoelectron diffraction experiment, as discussed by H. Daimon, T. Nakatani, S. Imada, S. Suga, Y. Kagoshima, and T. Miyahara, *Jpn. J. Appl. Phys.* **32,** L1480 (1993).
33. The handedness of circularly polarized light is not uniquely defined. We follow Feynman and the convention used in particle physics. See R. P. Feynman and R. B. Leighton and M. Sands, *The Feynman Lectures on Physics, Vol. I, Part 2*, Addison-Wesley Publishing Co., Inc., Reading, MA, 1964.
34. J. C. Slater and G. F. Koster, *Phys. Rev.* **94,** 1498 (1954).
35. D. A. Papaconstantopoulos, *Handbook of the Band Structure of Elemental Solids*, Plenum Publishing Co., New York, 1986.
36. J. Stöhr, *NEXAFS Spectroscopy*, Vol. 25 of *Springer Series in Surface Sciences*, Springer-Verlag, Heidelberg, 1992.
37. A. Abragam and B. Bleaney, *Electron Paramagnetic Resonance of Transition Ions*, Clarendon Press, Oxford, 1970.
38. P. Bruno, in *Magnetismus von Festkörpern und Grenzflächen*, KFA Jülich, Jülich, 1993, p. 24.1.
39. G. H. O. Daalderop, P. J. Kelly, and M. F. H. Schuurmans, *Phys. Rev. B* **50,** 9989 (1994).
40. H. Dürr and G. van der Laan, *Phys. Rev. B* **54,** 760 (1996).
41. R. A. Reck and D. L. Fry, *Phys. Rev.* **184,** 492 (1969).
42. R. Wu, D. Wang, and A. J. Freeman, *Phys. Rev. Lett.* **71,** 3581 (1993).
43. R. Wu and A. J. Freeman, *Phys. Rev. Lett.* **73,** 1994 (1994).
44. L. Tröger, D. Arvanitis, K. Baberschke, H. Michaelis, U. Grimm, and E. Zschech, *Phys. Rev. B* **46,** 3283 (1992).
45. L.-C. Duda, J. Stöhr, D. C. Mancini, A. Nilsson, N. Wassdahl, J. Nordgren, and M. G. Samant, *Phys. Rev. B* **50,** 16,758 (1994).
46. M. van Veenendahl, J. B. Goedkoop, and B. T. Thole, *Phys. Rev. Lett.* **77,** 1508 (1996).
47. S. S. P. Parkin, *Phys. Rev. Lett.* **71,** 1641 (1993).
48. M. G. Samant, J. Stöhr, S. S. P. Parkin, G. A. Held, B. D. Hermsmeier, F. Herman, M. van Schilfgaarde, L.-C. Duda, D. C. Mancini, N. Wassdahl, and R. Nakajima, *Phys. Rev. Lett.* **72,** 1112 (1994).
49. A. Nilsson, J. Stöhr, T. Wiell, M. Aldén, P. Bennich, N. Wassdahl, M. Samant, S. S. P. Parkin, N. Mårtensson, J. Nordgren, B. Johansson, and H. L. Skriver, *Phys. Rev. B* **54,** 2917 (1996).
50. S. Pizzini, F. Baudelet, D. Chandesris, A. Fontaine, H. Magnan, J. M. George, F. Petroff, A. Barthélemy, A. Fert, R. Loloee, and P. A. Schroeder, *Phys. Rev. B* **46,** 1253 (1992).
51. J. H. V. Vleck, *Phys. Rev.* **52,** 1178 (1937).

52. D. Weller, Y. Wu, J. Stöhr, M. G. Samant, B. D. Hermsmeier, and C. Chappert, *Phys. Rev. B* **49,** 12,888 (1994).
53. D. Weller, J. Stöhr, R. Nakajima, A. Carl, M. G. Samant, C. Chappert, R. Mégy, P. Beauvillain, P. Veillet, and G. Held, *Phys. Rev. Lett.* **75,** 3752 (1995).
54. P. Bruno, *Phys. Rev. B* **39,** 865 (1989).
55. D. Wang, R. Wu, and A. J. Freeman, *J. Magn. Magn. Mater.* **129,** 237 (1994).
56. C. T. Chen, Y. U. Idzerda, H. Lin, G. Meigs, A. Chaiken, G. A. Prinz, and G. H. Ho, *Phys. Rev. B* **48,** 642 (1993).
57. S. Pizzini, A. Fontaine, C. Giorgetti, E. Dartyge, J. F. Bobo, M. Piecuch, and F. Baudelet, *Phys. Rev. Lett.* **74,** 1470 (1995).
58. G. Schütz, R. Wienke, W. Wilhelm, W. Wagner, P. Kienle, R. Zeller, and R. Frahm, *Z. Phys. B* **75,** 495 (1989).
59. G. Schütz, H. Ebert, P. Fischer, S. Rüegg, and W. B. Zeper, *Mater. Res. Soc. Symp. Proc.* **231,** 77 (1992).
60. R. Wienke, G. Schütz, and H. Ebert, *J. Appl. Phys.* **69,** 6147 (1991).
61. G. R. Harp, S. S. P. Parkin, W. L. O'Brien, and B. P. Tonner, *Phys. Rev. B* **51,** 12,037 (1995).
62. M. Tischer, D. Arvanitis, T. Yokoyama, T. Lederer, L. Tröger, and K. Baberschke, *Surf. Sci.* **307–309,** 1096 (1994).
63. W. L. O'Brien and B. P. Tonner, *Surf. Sci.* **334,** 10 (1995).
64. A. Aspelmeier, M. Tischer, M. Farle, M. Russo, K. Baberschke, and D. Arvanitis, *J. Magn. Magn. Mater.* **146,** 256 (1995).
65. V. Chakarian, Y. U. Idzerda, H. Lin, C. Gutierrez, G. A. Prinz, G. Meigs, and C. T. Chen, *Phys. Rev. B* **53,** 11,313 (1996).
66. C. M. Schneider, K. Holldack, M. Kinzler, M. Grunze, H. P. Oepen, F. Schäfers, H. Petersen, K. Meinel, and J. Kirschner, *Appl. Phys. Lett.* **63,** 2432 (1993).
67. The data shown have been corrected for incomplete saturation effects, as discussed in H. Dürr, G. van der Laan, and B. T. Thole, *Phys. Rev. Lett.* **76,** C3464 (1996).

Received October 26, 1996; accepted for publication July 1, 1997

Joachim Stöhr *IBM Research Division, Almaden Research Center, 650 Harry Road, San Jose, California 95120 (stohr@almaden.ibm.com).* Dr. Stöhr is a Research Staff Member in the Science and Technology Department at the Almaden Research Center. He received a Vordiplom degree in physics from Bonn University in 1968 and studied as a Fulbright scholar in physics at Washington State University in 1969 and 1970, receiving an M.S. degree in 1971. He received a Dr. rer. nat. degree from the Technical University Munich in 1974. In 1975 and 1976 he was a Postdoctoral Fellow at Lawrence Berkeley National Laboratory and joined the Stanford Synchrotron Radiation Laboratory as a Staff Scientist in 1977. In 1981 he became a Senior Staff Physicist at the EXXON Corporate Research Science Laboratory. He left EXXON in 1985 to join the IBM Almaden Research Center, where he managed various groups, including the Magnetic Materials and Phenomena Department, from 1991 to 1994. Dr. Stöhr is the author of the book *NEXAFS Spectroscopy* and more than 200 scientific publications, mostly in the area of surface science. He is a Consulting Professor in the Electrical Engineering Department at Stanford University, a Consulting Professor at the Stanford Synchrotron Radiation Laboratory, and an Adjunct Professor in Physics at Uppsala University, Sweden. He has been a Fellow of the American Physical Society since 1988.

Reiko Nakajima *Department of Materials Science and Engineering, Stanford University, Stanford, California 94305 (nakajima@leland.stanford.edu).* Ms. Nakajima received an A.B. degree in physics from Princeton University in 1992. She is currently a graduate student in the Materials Sciences Department at Stanford University in the group of Professor Robert White. Her dissertation concerns X-ray magnetic circular dichroism spectroscopy in transition-metal thin films.